



# Argon-seeded plasma exposure and oxidation performance of tungsten-chromium-yttrium smart alloys

Janina Schmitz<sup>1,2</sup> · Andrey M. Litnovsky<sup>1</sup> · Felix Klein<sup>1</sup> · Xiaoyue Tan<sup>1,3</sup> · Uwe Breuer<sup>4</sup> · Marcin Rasinski<sup>1</sup> · Stephan Ertmer<sup>1</sup> · Arkadi Kreter<sup>1</sup> · Jesus Gonzalez-Julian<sup>1</sup> · Martin Bram<sup>1</sup> · Jan Willem Coenen<sup>1</sup> · Christian Linsmeier<sup>1</sup>

Received: 3 April 2019 / Revised: 6 May 2019 / Accepted: 6 May 2019 / Published online: 21 June 2019  
© The Author(s) 2019

## Abstract

Tungsten-chromium-yttrium (WCrY) smart alloys are foreseen as the first wall material for future fusion devices such as Demonstration Power Plant (DEMO). While suppressing W oxidation during accidental conditions, they should behave like pure W during plasma operation due to preferential sputtering of the lighter alloying elements Cr, Y, and W enrichment of the surface. In this paper, the erosion performance of WCrY and W samples simultaneously exposed to deuterium (D) plasma with the addition of 1% of the projectile ions being argon (Ar) ions at an ion energy of 120 eV is compared. With reference to the previous experiments at 120 eV in pure D plasma, the erosion for both WCrY and W is enhanced by a factor of ~7. Adding Ar to the D plasma suppresses significant W enrichment previously found for pure D plasma. To investigate the impact of the plasma exposure onto the oxidation performance, plasma-exposed and non-exposed reference samples were oxidised in a dry atmosphere. Results show, on the one hand, that the oxidation suppression of WCrY in comparison to pure W is preserved during the plasma performance. On the other hand, it becomes evident that edge effects imposed by the geometry of the samples used in plasma experiments play a significant role for the oxidation behaviour.

**Keywords** Tungsten-based alloys · Plasma-facing material · Smart alloys · DEMO

## 1 Introduction

The first wall of Demonstration Power Plant (DEMO) will presumably be made up of tungsten (W) [1]. W possesses various advantages, such as a high melting point, low erosion yields, and low tritium retention. These advantages make W a suitable candidate for the material challenges posed by plasma-wall interaction processes as described, e.g., in Ref. [2]. Yet, there are some drawbacks in using W as an armour material. Besides its inherent brittleness,

W oxidises easily when coming into contact with oxygen (O). For reactor accidents where the cooling system fails and the wall heats up due to neutron decay heat (loss-of-coolant-accident: LOCA), additional air ingress may occur and tungsten oxide (WO<sub>3</sub>) may form. Wall temperatures of more than 1000 °C for several months [3] lead to the sublimation of WO<sub>3</sub>. Since W has previously been activated by neutrons during the plasma operation, the radioactive material is then mobilised and released to the environment. To ascertain the intrinsic safety of a future fusion power plant by preventing the release of radioactive materials, W-based smart alloys are currently developed. These alloys aim at preserving W-like erosion behaviours during plasma operation while suppressing oxidation in case a LOCA occurs.

So far, the most promising alloy systems feature chromium (Cr) as a passivating element as well as small amounts of yttrium (Y) as an active element improving the oxidation resistance. Y facilitates the Cr transport towards the alloy's surface during oxidation; it adds to the stability of the oxide scale and supports the formation of a continuously growing,

✉ Janina Schmitz  
jan.schmitz@fz-juelich.de

<sup>1</sup> Forschungszentrum Juelich GmbH, Institut fuer Energie- und Klimaforschung, 52425 Juelich, Germany

<sup>2</sup> Department of Applied Physics, Ghent University, 9000 Ghent, Belgium

<sup>3</sup> School of Materials Science and Engineering, Hefei University of Technology, Hefei 230009, China

<sup>4</sup> Forschungszentrum Juelich GmbH, Institut fuer Engineering und Analytik, 52425 Juelich, Germany

well-adhering and dense  $\text{Cr}_2\text{O}_3$  layer [4]. It was shown that WCrY-systems can suppress the oxidation rate significantly compared to that of pure W [5, 6].

During plasma operation, the W-like erosion behaviours shall be preserved by preferential sputtering of the lighter alloying elements Cr and Y, leaving the plasma facing a pure W surface. With the aim of testing the performance of WCrY and reference W samples under DEMO-relevant plasma conditions, experiments were conducted in the linear plasma device PSI-2 [7] at Forschungszentrum Juelich (FZJ). The first two experiments used steady-state pure deuterium (D) plasma at ion energies of 120 eV and 220 eV, respectively. Results were reported in Ref. [8]. For the exposure at 220 eV, W sputtering by D and Cr transports to the surface led to an enhanced volume loss of WCrY samples as compared to simultaneously exposed pure W samples. At 120 eV, depletion of alloying elements at the samples' surfaces was accompanied by a significant W enrichment, resulting in similar erosion yields for pure W and WCrY.

For the operation of next-step fusion devices such as DEMO, seeding of impurities for radiative cooling may be necessary [9]. Possible impurity species are, among others, argon (Ar), krypton and xenon, all of which possess a higher sputter yield than that of D. To investigate the impact of impurity seeding on WCrY alloys, an exposure of WCrY and W samples was performed in steady-state D plasma in PSI-2. Based on calculations presented in Ref. [10, 11] Ar was added as an impurity species, so that 1% of the D ion beam consisted of Ar ions. Results and implications of the experiment are reported in this paper. Since smart alloys should preserve their passivation properties after plasma operation, the oxidation performance of the samples exposed in PSI-2 was tested. This was done using a thermogravimetric analyser in FZJ. Results of oxidation studies of samples exposed to the here-reported Ar-seeded D as well as to pure D plasma, both at 120 eV, are presented.

## 2 Experimental

### 2.1 Plasma exposure

The WCrY samples used for this as well as for previous plasma experiments were produced by mechanical alloying (MA) and compacted using Field-Assisted Sintering Technology (FAST) [12] with a composition of W-11.4 wt.% Cr-0.6 wt.% Y. Four WCrY samples (named by WCrY1, WCrY2, WCrY3 and WCrY4) were exposed simultaneously with 4 W samples (named by W1, W2, W3, and W4) produced according to ITER specifications [13]. Parameters for the sintering process are a heating ramp of  $200\text{ }^\circ\text{C min}^{-1}$ , a maximum pressure of 50 MPa, and no holding time after the maximum temperature of  $1460\text{ }^\circ\text{C}$  is reached. Furthermore, samples are cooled at a rate of  $300\text{ }^\circ\text{C min}^{-1}$ . The microstructure obtained after sintering is characterised by submicrometer-sized grains of W-Cr solid solution with finely dispersed yttria particles with a size of  $< 150\text{ nm}$  [5]. More details on the sample production and resulting microstructure can be found in Ref. [5]. For the sintered WCrY samples, WCrY1–4 relative densities of 98.6%, 91.2%, 93.2%, and 98.4% of the theoretical 100% density, assuming a composition of W-11.4 wt.% Cr-0.6 wt.% Y, are obtained. The measured relative density of the W samples is more than 99%. The density is measured by immersing the samples into ethanol and using the Archimedes principle. The WCrY ingots obtained after sintering as well as the reference W samples are first cut by wire erosion (see Fig. 1) to fit the sample holder geometry (shown in Fig. 2). Then, all samples are manually ground to remove residual impurities from cutting. For grinding silicon-carbide (SiC) papers used, in the final grinding step SiC 1200 paper is used, resulting in a surface roughness of  $\sim 30\text{ nm}$ . After the sample preparation, the shape of the WCrY sample is depicted in Fig. 1a. The red and green coloured areas on the W sample indicate the plasma-facing surface and the analysis region for secondary

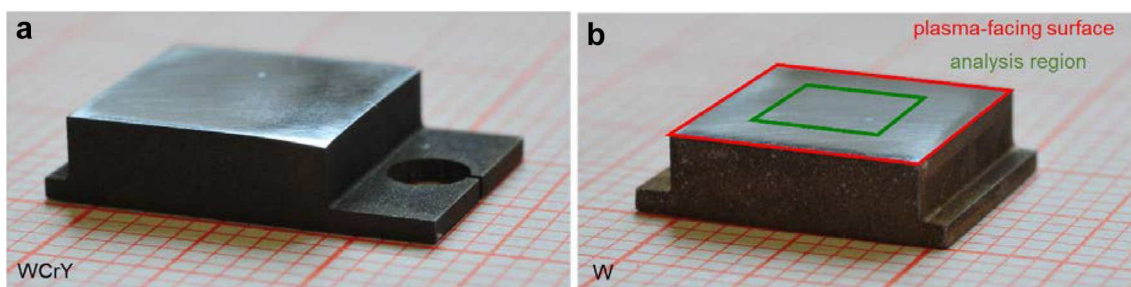


**Fig. 1** Pictures of **a** WCrY and **b** W samples with the typical geometry for plasma exposure. The hole is added to the WCrY geometry for oxidation studies



**Fig. 2** Target holder with radially placed WCrY and W samples for exposure in PSI-2

ion mass spectroscopy (SIMS), focussed ion beam (FIB), and Dektak measurements. The W sample shape is displayed in Fig. 1b. W and WCrY sample geometries are identical except for the hole added on top of the WCrY for hanging the sample in the furnace during the oxidation experiment. For all samples, the plasma-facing surface spans  $\sim 1 \text{ cm} \times 1 \text{ cm}$ .

The following methods are used for analyses before and after plasma exposure: a Sartorius MSA225P microbalance with a resolution of  $10 \mu\text{g}$  is used to infer the mass loss  $\Delta m$  after plasma exposure. The scanning electron microscope-focussed ion beam (SEM-FIB) system Carl Zeiss Cross-Beam XB540 is used to take SEM images of the surface and of the microstructure. This device is further used for energy-dispersive X-ray spectroscopy (EDX). For imaging the microstructure first, a crater is cut orthogonally to the sample surface with a focussed ion beam (FIB). Using the FIB crater, it is possible to obtain an additional erosion measurement: the surface recession, i.e., the thickness of the plasma-eroded layer,  $d_e$ . This value is measured by

creating equidistant marker lines inside the cut and comparing the distance between uppermost marker and the sample surface before and after plasma exposure. Such a prepared FIB cut before plasma is shown in Fig. 3a. Time-of-flight secondary ion mass spectroscopy (ToF-SIMS, IonToF IV) is used for analysing the depth-resolved target composition and the Dektak 6 M stylus profilometer with a tip radius of  $2.5 \mu\text{m}$  for measuring the surface roughness  $R_a$ . A more detailed description of the analytic techniques used can be found in Ref. [8]. During the plasma exposure, different in situ diagnostics are used: with a Langmuir probe, the plasma parameters such as the ion flux incident to the target or the plasma potential are monitored. With the aid of an infrared (IR) camera, the temperature of the sample surfaces is measured. For this purpose, the emissivity is calibrated by heating the samples and comparing the temperatures of the holder's thermocouple and those of the samples as measured by the IR camera before starting the plasma. Spectroscopy is used to monitor the relative signal evolution of neutral W (W1 at a wavelength of  $429.5 \text{ nm}$ ) and neutral Cr (CrI at a wavelength of  $427.5 \text{ nm}$ ) line radiation emitted by sputtered particles in front of the target during the experiment.

Plasma parameters for this exposure are displayed in Table 1. All samples are placed axially symmetric onto the sample holder made of pure W. This geometry fits the hollow plasma profile of PSI-2 [7], so that all samples are exposed to as similar plasma conditions as possible. However, inhomogeneities in the plasma profile can lead to a variation of the flux and fluence between samples. Furthermore, residual oxygen, which is assumed to be of the order of 0.1% of the plasma ion flux, adds to the erosion of the samples. Residual oxygen, which is assumed to be significantly below

**Table 1** Plasma parameters in PSI-2

Plasma	Ion energy/ eV	Ion flux/ (ions $\text{m}^{-2} \text{s}^{-1}$ )	Ion fluence/ (ions $\text{m}^{-2}$ )	Sample temperature/ $^{\circ}\text{C}$
99% D, 1% Ar	120	$2.8 \times 10^{21}$	$2 \times 10^{25}$	620–720

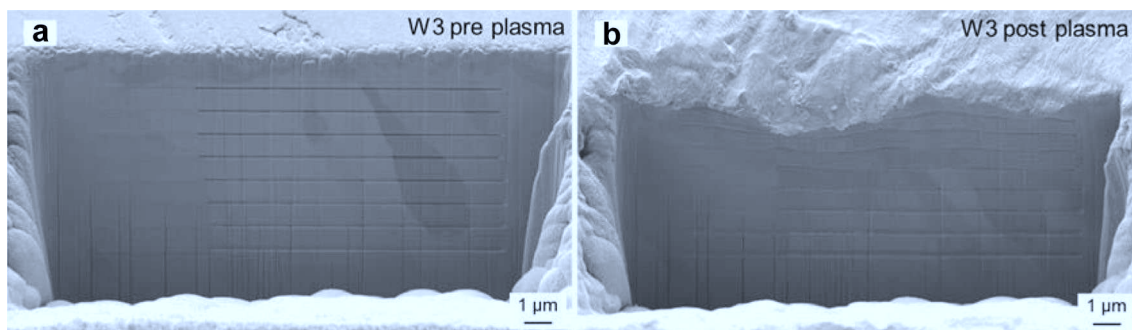


**Fig. 3** SEM images of FIB craters with markers on W3 **a** before and **b** after plasma exposure

1% of the plasma ion flux, is not accounted for in the plasma composition in Table 1. Sample holders and samples are displayed in Fig. 2. The samples' surfaces are mounted in a way that they protrude from the mask's surface to minimise re-deposition from material eroded from the mask.

## 2.2 Oxidation testing

Oxidation experiments are performed in the thermogravimetric analyser TAG-16/18 from SETARAM instrumentation. This analyser is built as a dual furnace, one furnace containing the investigated sample and the other containing an inert product with the same volume as the sample to counteract buoyancy effects. The temperature and the atmosphere inside the furnace can be controlled. Samples and the inert products are hung into the furnace tubes using a platinum wire. The oxidation rate of a sample is determined by measuring the mass increase as oxygen from the atmosphere reacts with the sample. More details on the oxidation testing setup can be found in Ref. [14].

Oxidation experiments reported in this paper took place at 1000 °C in an atmosphere containing 80 volume (vol.%) Ar + 20 vol.% O at 0.1 MPa. Due to the geometry used for PSI-2 exposure, it is not possible to grind the samples meant for plasma exposure from all sides (see Fig. 1a). Smart alloy samples not meant for plasma exposure but specifically for determining oxidation rates have a standardised cubic shape and are ground from all sides [14]. Wire erosion leads to deposition of the wire material onto the samples. Due to the geometry of the PSI-2 samples, not all remnants from wire erosion cutting can be removed during grinding. Moreover, it is stated that sample edges or other surface defects such as scratches are prone to the formation of W-containing oxides [14]. Thus, a sample with many edges and on top with remaining dirt from wire erosion is expected to show a bad oxidation behaviour. For this reason, two WCrY reference samples with the PSI-2 geometry were oxidised without being exposed to plasma before, so that the oxidation

rates of non-plasma-exposed and plasma-exposed samples can be compared.

The oxide formation causes a mass increase of the sample. This mass increase is a measure of the sample's oxidation performance. Ideally, the mass should not increase after the protective oxide layer forms. If the oxidation of the sample slows down, the mass increase slows down. If the mass remains constant, the gradient of the mass change becomes zero. When a dense and closed oxide scale on the surface is formed and the sample is chemically inactive (passive), self-passivation is reached. For further oxidation at the surface, metal ions need to diffuse through the dense scale to react with the atmosphere. The rate of oxidation is determined by diffusion of metal ions through the scale and is, therefore, significantly slowed down. Towards reaching this state, the gradient of mass change steadily decreases and converges to a stable value.

## 3 Results

### 3.1 Plasma exposure

Results for the mass loss  $\Delta m$ , the measured surface recession  $d_e$ , as well as the calculated one and the roughness  $R_a$  (arithmetic average of the roughness profile) of all samples are displayed in Table 2. The calculated surface recession is obtained by dividing the mass loss  $\Delta m$  by the material's density  $\rho$ , 19.25 g cm<sup>-3</sup> for W, and 15.87 g cm<sup>-3</sup> for WCrY, and multiplying by the area  $A$  of the plasma-facing surface:

$$d_e = \Delta m A / \rho. \quad (1)$$

$\bar{W}$  and  $\overline{\text{WCrY}}$  are the average values of all measurements over the W and WCrY samples, respectively. In general, the weight loss for the WCrY samples is less than that of the pure W samples: the average weight losses are  $660 \pm 40$  mg for W and  $500 \pm 70$  mg for WCrY, while the measured surface recession is similar with  $0.30 \pm 0.08$   $\mu\text{m}$  for W and  $0.34 \pm 0.05$   $\mu\text{m}$  for WCrY. This finding can be explained by

**Table 2** Weight loss and roughness before and after plasma for the individual W and WCrY samples and the average values for W ( $\bar{W}$ ) and WCrY ( $\overline{\text{WCrY}}$ )

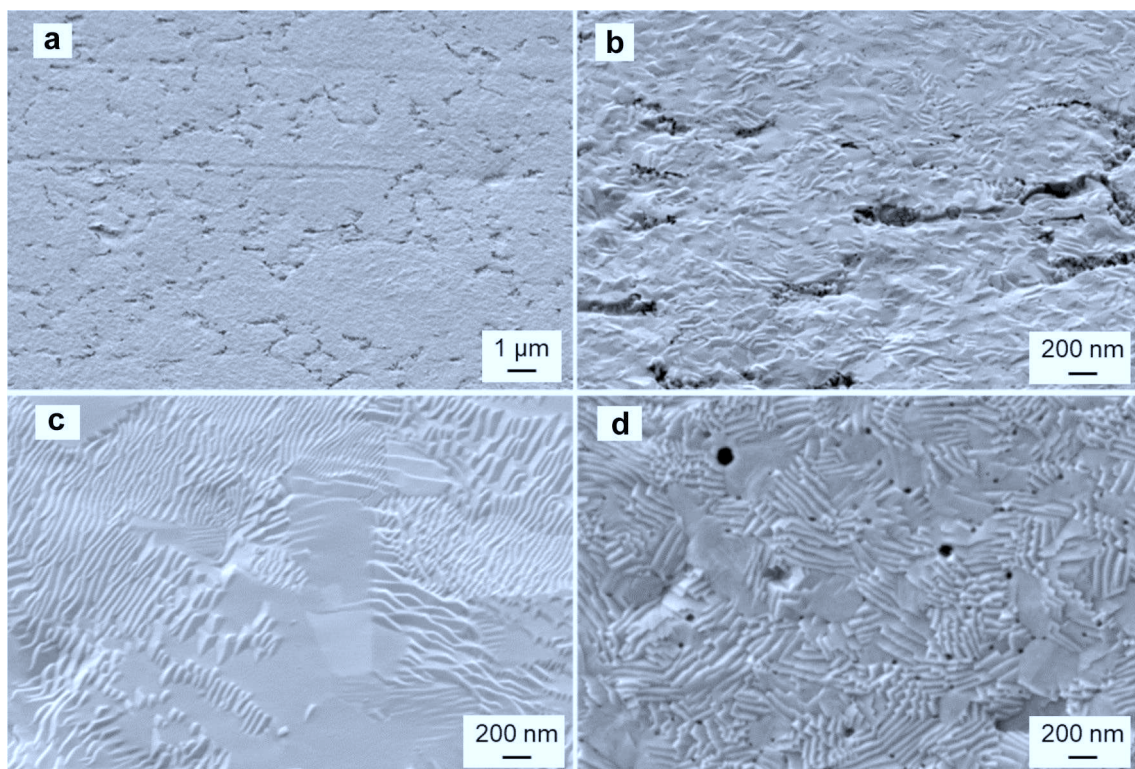
Sample	$\Delta m/\mu\text{g}$	$R_a$ before/nm	$R_a$ after/nm	$d_e$ measured/ $\mu\text{m}$	$d_e$ calculated/ $\mu\text{m}$
W1	$640 \pm 10$	$39 \pm 0$	$40 \pm 5$	Not available	$0.32 \pm 0.01$
W2	$710 \pm 10$	$23 \pm 0$	$31 \pm 2$	$0.30 \pm 0.08$	$0.37 \pm 0.01$
W3	$680 \pm 10$	$30 \pm 1$	$34 \pm 7$	Not available	$0.35 \pm 0.01$
W4	$640 \pm 10$	$25 \pm 1$	$29 \pm 6$	Not available	$0.33 \pm 0.01$
WCrY1	$500 \pm 10$	$34 \pm 0$	$25 \pm 2$	$0.32 \pm 0.08$	$0.32 \pm 0.01$
WCrY2	$580 \pm 10$	$25 \pm 0$	$30 \pm 5$	$0.28 \pm 0.04$	$0.37 \pm 0.01$
WCrY3	$520 \pm 10$	$17 \pm 0$	$21 \pm 0$	$0.39 \pm 0.06$	$0.33 \pm 0.01$
WCrY4	$380 \pm 10$	$50 \pm 1$	$35 \pm 0$	$0.35 \pm 0.06$	$0.24 \pm 0.01$
$\bar{W}$	$660 \pm 40$	$29 \pm 6$	$34 \pm 4$	$0.30 \pm 0.08$	$0.34 \pm 0.02$
$\overline{\text{WCrY}}$	$500 \pm 70$	$32 \pm 12$	$28 \pm 5$	$0.34 \pm 0.05$	$0.31 \pm 0.05$

the low density  $\rho$  of the alloy WCrY. Average calculated and measured surface recession values  $d_e$  agree within error bars. Measuring the surface recession using the FIB-generated markers was only possible for W2. Samples W1, W3, and W4 feature deformations after plasma exposure, as shown in Fig. 3b for W3. The origin of the deformations is not known. One assumption is that they arise from induced mechanical stresses during production of the W plate from which the samples are cut. On average, the surface roughness is slightly increased or remains stable for most samples. This becomes also evident when looking at the surface of W3 post-plasma in the aforementioned figure: the surface features a wave-like structure, whereas, before plasma, it was smooth besides scratches from grinding. The scratches from grinding remain after plasma and still mainly determine the surface roughness.

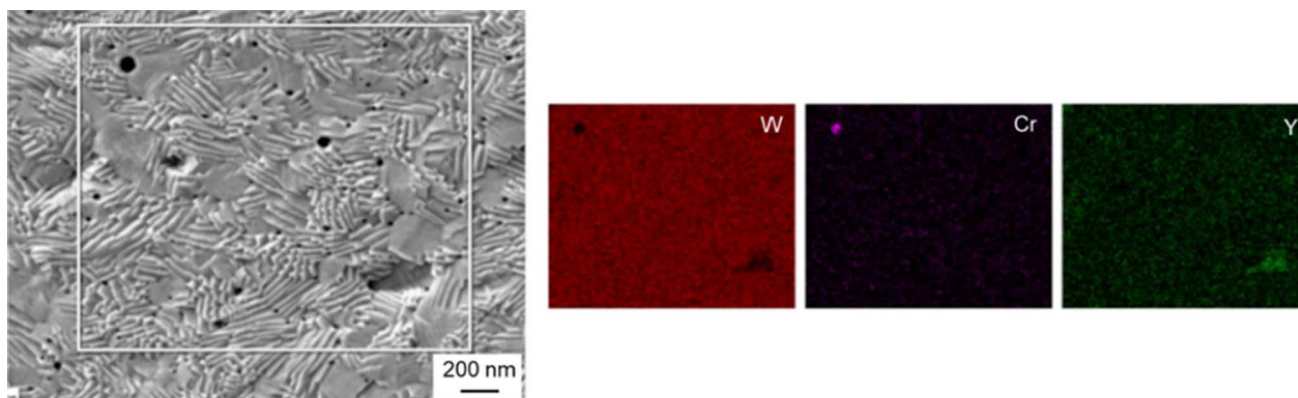
Figure 4a,b shows SEM images of WCrY exposed to D + Ar plasma in the experiment at different magnifications. For comparison, the surface of a simultaneously exposed W surface is shown (Fig. 4c) as well as a WCrY sample exposed to pure D plasma at an ion energy of 120 eV in an earlier reported experiment (Fig. 4d) [8]. SEM images of the WCrY sample after D + Ar plasma show elongated craters along the grain boundaries and small black holes on the surface. These are very similar but not as pronounced

as for the sample exposed to pure D plasma in Fig. 4d. As the size of the yttrium and oxide containing (YO)-particles amounts to typically a few tenth of nm in the WCrY microstructure, these small black holes are assumed to be preferentially sputtered YO particles. Furthermore, the craters are assumed to be caused by the superficial depletion of Cr. EDX results on the surface of the sample shown in Fig. 4d are shown in Fig. 5. The results support the assumptions of Y and Cr depletion. The information depth for EDX is  $\sim 150$  to  $200$  nm in W and WCrY, respectively. Hence, EDX shows Y and Cr beneath the small black hole and big crater, respectively. On the W samples, no holes nor craters were found, as shown in Fig. 4c. Pure W samples are sputtered down homogeneously as they only consist of one element, unlike the WCrY samples where Cr and Y are sputtered preferentially. On all exposed W and WCrY samples, wave-like structures correlating with the grain orientation can be seen after plasma exposure.

The depth-resolved elemental composition of WCrY as measured by SIMS before and after plasma is shown in Fig. 6a, b. The intensity of the signals for W, Cr, and Y is normalised to be 1 in the bulk material, i.e., at the last measured point at  $\sim 600$  nm depth inside the sample. Before plasma exposure, the signals of Y and Cr show a sharp increase towards the surface. This peak vanishes

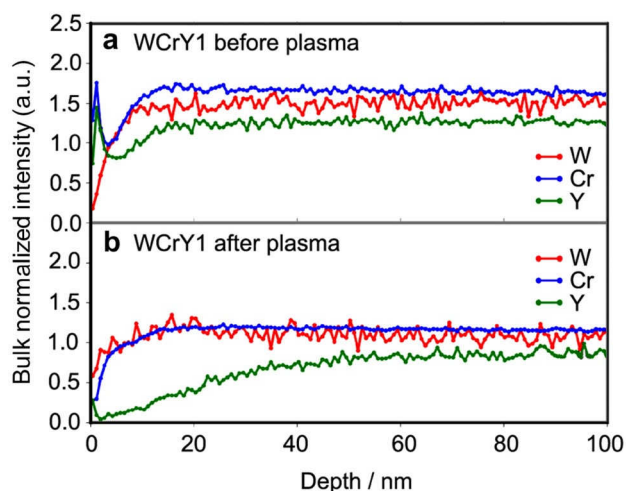


**Fig. 4** SEM images of the surface of WCrY3 after plasma exposure at a magnification of **a** 5 K and **b** 25 K and **c** of W1 after plasma exposure; **d** a WCrY sample after plasma exposure to pure D at an ion energy of 120 eV

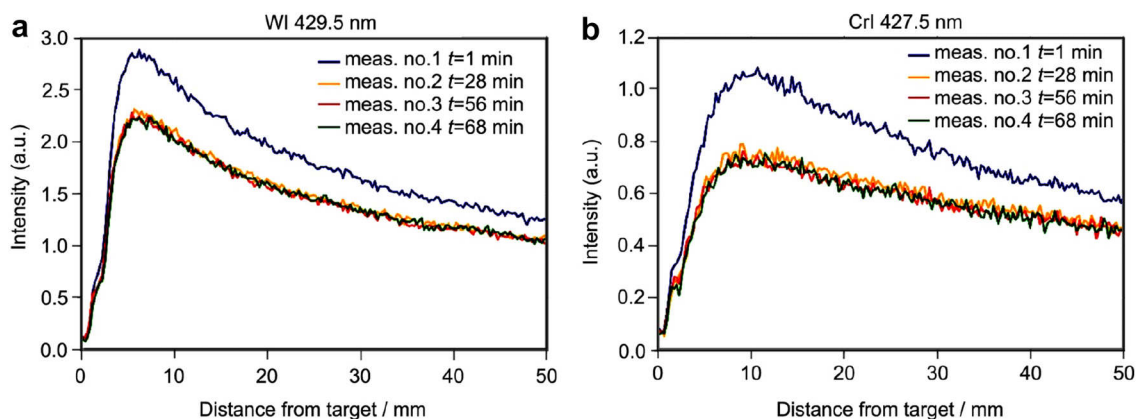


**Fig. 5** EDX surface map of the elements W, Cr, and Y of a WCrY sample exposed to pure D plasma at an ion energy of 120 eV

after plasma exposure. It can be seen that the relative signal evolution for each element is changed only up to a depth of ~20 to 50 nm below the surface. Whereas the Y

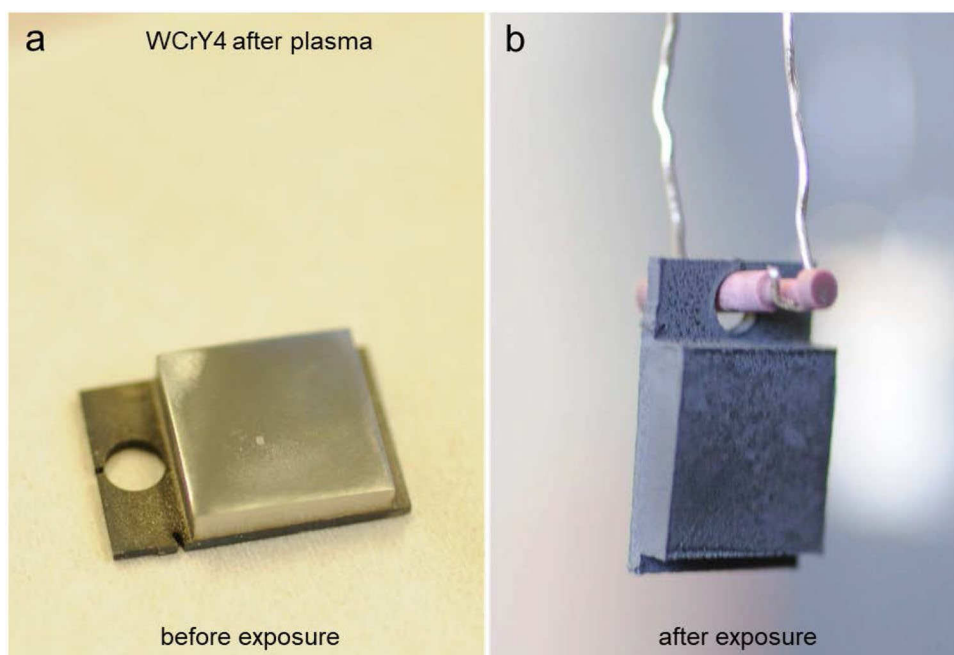


**Fig. 6** Elemental composition of WCrY1 measured by SIMS **a** before and **b** after plasma exposure



**Fig. 7** Spectroscopy measurements of **a** WI at a wavelength of 429.5 nm and **b** CrI at a wavelength of 427.5 nm during plasma exposure

**Fig. 8** Pictures of the sample WCrY4 **a** before and **b** after isothermal oxidation in dry air



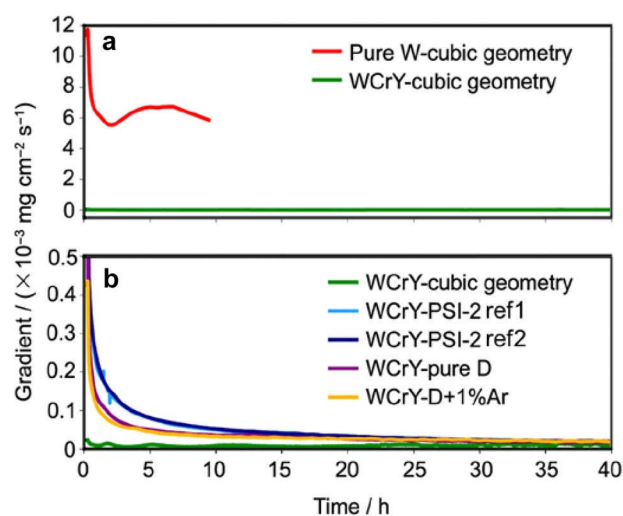
intensities of meas no. 2–4. Measurements 2–4 were taken at 28, 56, and 68 min after plasma start, respectively. No changes in the signal intensities are visible, and thus, during the whole plasma exposure, W as well as Cr is eroded from the samples and the target holder, which is made of pure W.

Figure 8a and 8b show pictures of WCrY4 before and after plasma exposure, respectively.

### 3.2 Oxidation testing

In Fig. 9a, the oxidation performance of a cubic pure W sample is compared to that of a cubic WCrY sample with the optimum composition of W-11.4 wt.%Cr-0.6 wt.% Y. The W sample fails, the curve stops at ~9 h, at this point, and the sample loses its initial cubic shape. In contrast, the gradient of the WCrY sample starts at a value of  $\sim 2 \times 10^{-5} \text{ mg cm}^{-2} \text{ s}^{-1}$ . In comparison to the pure W sample, oxidation is suppressed successfully by three orders of magnitude. The oxidation performance is shown for up to 40 h. During this time, the gradient remains approximately constant at  $\sim 2 \times 10^{-5} \text{ mg cm}^{-2} \text{ s}^{-1}$  and does not rise again, as it is the case for the W sample after ~2 h. A rising gradient of the mass change means a sudden increase of the oxidation rate, e.g., due to the breaking apart of the sample a bigger surface can be accessed by oxygen. In contrast, the stable gradient of the cubic WCrY sample means that the oxidation rate is constant. A dense oxide scale forms resulting in a steady and slow mass gain.

The curves of the two reference PSI-2 WCrY samples are shown in Fig. 9b and are labelled PSI-2 ref1 and ref2. The



**Fig. 9** Gradient of the mass change in  $\text{mg cm}^{-2} \text{ s}^{-1}$  during isothermal oxidation in dry air at 1000 °C in an atmosphere containing 80 vol.% Ar + 20 vol.% O at 0.1 MPa. **a** Pure W and WCrY samples with a cubic geometry; **b** WCrY samples: with cubic geometry, with PSI-2 geometry and not exposed (PSI-2 ref1 and ref2), with PSI-2 geometry and exposed to pure D 120 eV (pure D) and to D with 1% Ar (D + 1% Ar)

y-scale of Fig. 9b is magnified in comparison to Fig. 9a, so that the differences between the different WCrY samples can be seen more clearly. One can see that although the gradient of the PSI-2 reference samples starts at a higher initial value than the cubic geometry sample, all three curves converge to a value of  $\sim 2 \times 10^{-5} \text{ mg cm}^{-2} \text{ s}^{-1}$  after 40 h. The edge

effects and the wire erosion remnants increase the mass gain at the beginning of the experiment. However, after ~20 h, the PSI-2 reference samples show a similar performance compared to one of the cubic WCrY sample. The same is true for the two samples exposed to plasma: WCrY-pure D, which is exposed to 120 eV pure D plasma reported in Ref. [8], and WCrY-D + 1% Ar, sample WCrY4 reported in this paper. These two plasma-exposed samples even show slightly better performances during the first 15–20 h of oxidation compared to the reference samples. We suspect that this improved performance of the plasma-exposed samples is a result of the plasma irradiation removing some dirt at the sample edges. As can be seen in Fig. 8, the sample keeps its shape, and the surface appears black due to the oxide formation.

Since the plasma-irradiated area of 1 cm<sup>2</sup> makes out only ~one-fourth of the total sample surface area and edge effects play a crucial role, it is difficult to judge on the oxidation performance of plasma-exposed samples compared to non-exposed samples. More in-depth investigations of the plasma-exposed and reference PSI-2 geometry samples are ongoing, i.e., SEM images of cross sections of the oxidised surfaces will be analysed and compared.

## 4 Discussion

To assess the performance under DEMO-relevant plasma conditions, W and WCrY samples were simultaneously exposed to D + 1%Ar plasma in PSI-2. Erosion measurements for W and WCrY show that while the average mass loss is reduced for WCrY compared to that of W, the surface recession is approximately similar for W and WCrY. The average calculated surface recession agrees with the measured one. This means that the reduced mass loss at the same surface recession can be explained by the lower density of the WCrY alloy compared to W. There was no strong Cr diffusion towards the surface leading to an increased surface recession as reported in Ref. [8]. Neither significant depletion of Cr nor an enrichment of W, as found for exposure to pure D plasma at 120 eV [8], was detected in this experiment. Although the SEM images of the WCrY surface after exposure show the signs of preferential sputtering of Y and Cr, no significant sign of depletion of Cr or enrichment of W can be seen from the SIMS analysis. Here, one has to take into account that the surface roughness of ~30 nm complicates the interpretation of the subsurface elemental composition by SIMS. Still, a clear depletion of Y is visible from the signal evolution. The very shallow depletion of Cr can be attributed to the more similar sputter yields for Ar on W and Cr than for D on W and Cr [15]: sputter thresholds for D on W and Cr are 230 and 35 eV, respectively, and 27 and 22 eV

for Ar on W and Cr, respectively. Both pure W and WCrY were sputtered more severely by the addition of 1% Ar to the D plasma, which can be explained by the increased sputter yields of Ar on W compared to D on W. According to Ref. [16], at an ion energy of 120 eV, the sputter yield  $Y$  (sputtered atoms/incoming ion) is ~0.1 for Ar on W, whereas it is 0.0 for D on W as 120 eV is below the threshold for D on W.

Whereas, in Ref. [8], a surface recession of ~0.2 µm was reported for W and WCrY at a fluence of  $1 \times 10^{26}$  ions m<sup>-2</sup>, the Ar seeding led to a surface recession of ~0.3 µm already at a fluence of  $2 \times 10^{25}$  ions m<sup>-2</sup>. Using the spectroscopy setup, sputtering of W and Cr was visible for all measurements during the exposure, whereas, in pure D, the Cr signal was too low to be detected [8]. We assume that, in both experiments, small amounts of residual oxygen were present in the plasma, and still higher yields for Ar compared to O make the Ar sputtering dominant for this experiment. Inhomogeneity in the plasma profile and slightly different sample heights in the order of fractions of an mm after cutting and grinding lead to slightly different sputtering conditions for all samples. Yet, by exposing in total eight samples, four W and four WCrY samples, the average erosion values allow a reliable judgement on the plasma performance of WCrY in comparison to pure W. The damaged W samples do not allow reliable measurements of the surface recession. The reason for the deformed W samples has to be investigated. One approach to avoid this damage is to pre-anneal samples to release stresses. However, the mass loss measurements are not altered by the deformations.

Comparing a cubic pure W sample with a cubic WCrY sample with the optimum composition shows that WCrY successfully suppresses W oxidation and impressively enhances the failure resistance of the material. Edges added due to the PSI-2 geometry and remnants from wire erosion lead to an increased mass gain for the non-exposed reference and plasma-exposed WCrY samples. Still after 40 h of oxidation, the gradient of the mass change of all WCrY samples converges to the same value of  $\sim 2 \times 10^{-5}$  mg cm<sup>-2</sup> s<sup>-1</sup>. As shown in Fig. 9, the green curve of the cubic WCrY reference sample lies slightly below the curves of all other samples. Hence, effects due to the addition of more edges and caused by the cutting process are not quite levelled out after 40 h of oxidation. Still, all curves are equally flat and do not rise as the oxidation time increases.

## 5 Summary and outlook

The addition of 1% of Ar to D plasma at an ion energy of 120 eV leads to increased erosion for both W and WCrY. Compared to an exposure in pure D at the same ion energy, the surface recession was increased by a factor of more than

7. Adding seeding impurities such as Ar to hydrogen plasma degrades the benign erosion behaviour of W. Therefore, depletion of the alloying elements Cr and Y is only superficial in WCrY when Ar is added.

After 40 h of isothermal oxidation in dry air, the gradients in mass changes of the WCrY cubic sample, the PSI-2 reference samples, and the plasma-exposed samples converge to the same value. During plasma exposure, the good oxidation suppressing properties of WCrY smart alloys are conserved.

To investigate the DEMO-relevant material lifetime, experiments with increased fluence have to be conducted. At the sample temperatures of 620–720 °C, during this plasma exposure, no evidence for a strong Cr transport to the surface was found. At higher temperatures, thermal Cr diffusion could lead to an enhanced Cr transport as concentration gradients are induced by preferential sputtering at the surface. As a consequence, the temperature dependence of the erosion processes has to be investigated by conducting plasma exposures of W and WCrY at different temperatures and keeping the plasma parameters constant. In addition, effects due to mixed D, helium (He) irradiation on D retention, and microstructures will be the subject of future studies.

**Acknowledgements** This work was financially supported by the framework of the EURO fusion Consortium, the Euratom research and training programme 2014–2018 and 2019–2020 (Grant 633053), and the European Commission through the Erasmus Mundus International Doctoral College in Fusion Science and Engineering (FUSION-DC). The views and opinions expressed herein do not necessarily reflect those of the European Commission.

**Open Access** This article is distributed under the terms of the Creative Commons Attribution 4.0 International License (<http://creativecommons.org/licenses/by/4.0/>), which permits unrestricted use, distribution, and reproduction in any medium, provided you give appropriate credit to the original author(s) and the source, provide a link to the Creative Commons license, and indicate if changes were made.

## References

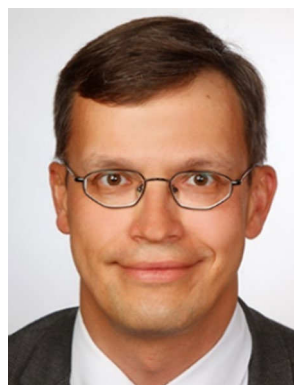
1. Stork D, Agostini P, Boutard JL, Buckthorpe D, Diegele E, Dudarev DL, English C, Federici G, Gilbert MR, Gonzalez S, Ibarra A, Linsmeier Ch, Puma AL, Marbach G, Morrisk PF, Packer LW, Raj B, Rieth M, Tran MQ, Ward DJ, Zinkle SJ. Developing structural, high-heat flux and plasma facing materials for a near-term DEMO fusion power plant: the EU assessment. *J Nucl Mater.* 2014;455(1–3):277.
2. Linsmeier Ch, Rieth M, Aktaa J, Chikada T, Hoffmann A, Hoffmann J, Houben A, Kurishita H, Jin XZ, Li MY, Litnovsky A, Matsuo S, von Müller A, Nikolic V, Palacios T, Pippan R, Qu DD, Reiser J, Riesch J, Shikama T, Stieglitz R, Weber T. Development of advanced high heat flux and plasma-facing materials. *Nucl Fusion.* 2017;57(9):092007.
3. Maisonnier D, Cook I, Sardain P, Boccaccini L, Bogusch E, Broden K, Di Pace L, Forrest R, Giancarli L, Hermesmeier S, Nardi C, Norajitra P, Pizzuto A, Taylor N, Ward D. The European power plant conceptual study. *Fusion Eng Des.* 2005;75–79:1173.
4. Wegener T, Klein F, Litnovsky A, Rasinski M, Brinkmann J, Koch F, Linsmeier Ch. Development of yttrium-containing self-passivating tungsten alloys for future fusion power plants. *Nucl Mater Energy.* 2016;9:394.
5. Litnovsky A, Wegener T, Klein F, Linsmeier Ch, Rasinski M, Kreter A, Tan XY, Schmitz J, Coenen JW, Mao YR. New oxidation resistant tungsten alloys for use in the nuclear fusion reactors. *Phys Scr.* 2017;T170:014012.
6. Klein F, Litnovsky A, Wegener T, Tan XY, Gonzalez-Julian J, Rasinski M, Schmitz J, Linsmeier Ch, Bram M, Coenen JW. Sublimation of advanced tungsten alloys under DEMO relevant accidental conditions. *Fusion Eng Des.* 2019. <https://doi.org/10.1016/j.fusengdes.2019.02.039>.
7. Kreter A, Brandt C, Brandt C, Huber A, Kraus S, Möller S, Reinhardt M, Schweer B, Sergienko G, Unterberg B. Linear plasma device PSI-2 for plasma-material interaction studies. *Fusion Sci Technol.* 2015;68:8.
8. Schmitz J, Litnovsky A, Klein F, Wegener T, Tan XY, Rasinski M, Mutzke A, Hansen P, Kreter A, Pospieszczyk A, Möller S, Coenen JW, Linsmeier Ch, Breuer U, Gonzales-Julian J, Bram M. WCrY Smart alloys as advanced plasma-facing materials—exposure to steady-state pure deuterium plasmas in PSI-2. *Nucl Mater Energy.* 2018;15:220.
9. Kallenbach A, Bernert M, Dux R, Casali L, Eich T, Giannone L, Herrmann A, McDermott R, Mlynec A, Müller HW, Reimold F, Schweinzer J, Sertoli M, Tardini G, Treutterer W, Viezzer E, Wenninger R, Wischmeier M, the ASDEX Upgrade Team. Impurity seeding for tokamak power exhaust: From present devices via ITER to DEMO. *Plasma Phys Control Fusion.* 2013;55(12):124041.
10. Wenninger R, Arbeiter F, Aubert J, Aho-Mantila L, Albanese R, Ambrosino R, Angioni C, Artaud JF, Bernert M, Fable E, Fasoli A, Federici G, Garcia J, Giruzzi G, Jenko F, Maget P, Mattei M, Maviglia F, Poli E, Ramogida G, Reux C, Schneider M, Sieglin B, Villone F, Wischmeier M, Zohm H. Advances in the physics basis for the European DEMO design. *Nucl Fusion.* 2015;55(6):063003.
11. Schmid K, Krieger K, Kukushkin A, Loarte A. DIVIMP modelling of tungsten impurity transport in ITER. *J Nucl Mater.* 2007;363–365:674.
12. Guillon O, Gonzalez-Julian J, Dargatz B, Kessel T, Schierner G, Räthel J, Herrmann M. Field-Assisted sintering technology/spark plasma sintering: mechanisms, materials, and technology developments. *Adv Eng Mater.* 2014. <https://doi.org/10.1002/adem.201300409>.
13. Barabash V. Material specification for the supply of tungsten plates for the ITER divertor IDM No. ITER D 2EDZJ4. ITER Document. 2019.
14. Klein F, Wegener T, Litnovsky A, Rasinski M, Tan XY, Gonzalez-Julian J, Schmitz J, Bram M, Coenen JW, Linsmeier Ch. Oxidation resistance of bulk plasma-facing tungsten alloys. *Nucl Mater Energy.* 2018;15:226.
15. Behrisch R, Eckstein W, editors. Sputtering by particle bombardment: experiments and computer calculations from threshold to MeV energies, volume 110 of topics in applied physics. Berlin: Springer-Verlag GmbH; 2007.
16. Eckstein W, García-Rosales C, Roth J, Ottenberger W. Sputtering data, Max-Planck-Institut für Plasmaphysik. Report IPP 9/82. 1993.

**Publisher's Note** Springer Nature remains neutral with regard to jurisdictional claims in published maps and institutional affiliations.



**Janina Schmitz** is a Ph.D. student at Forschungszentrum Juelich, Germany, at the Institute for Plasma Physics within the smart alloy research group since 2016. The Ph.D. project focusses on the development of tungsten-based alloys for future fusion power plants and is funded by the European Commission within the Erasmus Mundus International Doctoral College in Fusion Science and Engineering (FUSION-DC). Ms Schmitz pursued her MSc in fusion energy at the University of York, England.

During this time, she was able to gain experience working at the Joint European Torus (JET) fusion experiment in Culham, Oxfordshire. She aims to finish her Ph.D. thesis in 2019 and hopes to contribute with her work to the development of advanced tungsten-based materials.



**Dr. Andrey M. Litnovsky** is a graduate of Moscow State Engineering and Physics Institute (MEPhI) Russian Federation. His Ph.D. in physics and mathematics in 2001 was awarded for the work made in MEPhI and in Kurchatov institute, Moscow. Dr. Litnovsky works at the Forschungszentrum Juelich since 2002 studying edge plasmas of fusion devices, plasma-surface interactions processes, and developing diagnostic components for International Tokamak Experimental Reactor. As senior

scientist at the Forschungszentrum Juelich, Dr. Litnovsky is leading a number of European and International activities on plasma-wall interactions and plasma diagnostics, being a chief of operations of TEXTOR tokamak until the end of 2013. Among research projects, Dr. Litnovsky coordinates the development of advanced alloys for a future fusion power plant, leading the smart alloy research group at the Forschungszentrum Juelich.